1   **Towards an improved representation of carbonaceous aerosols over the**

2   **Indian monsoon region in a regional climate model RegCM**

4   Sudipta Ghosh[1], *Sagnik Dey[1,2], Sushant Das[3], Nicole Riemer[4], Graziano Giuliani[3], Dilip

5   Ganguly[1], Chandra Venkatraman[5], Filippo Giorgi[3], Sachchida Nand Tripathi[6], S.

6   Ramachandran[7], T.A. Rajesh[7], Harish Gadhavi[7], Atul Kumar Srivastava[8]

8   [1]Centre for Atmospheric Sciences, Indian Institute of Technology Delhi, India

9   [2]Centre of Excellence for Research on Clean Air, Indian Institute of Technology Delhi, India

10 [3]Earth System Physics Section, ICTP, Trieste, Italy

11 [4]Department of Atmospheric Sciences, University of Illinois at Urbana-Champaign, IL, USA

12 [5]Department of Chemical Engineering, Indian Institute of Technology Bombay, India

13 [6]Department of Civil Engineering, Indian Institute of Technology Kanpur, India

14 [7]Space and Atmospheric Sciences Division, Physical Research Laboratory, Ahmedabad, India

15 [8]Indian Institute of Tropical Meteorology, New Delhi Branch, India

17 ***Correspondence: sagnik@cas.iitd.ac.in**

19 **Keywords:** RegCM4; emission inventory; carbonaceous aerosols; model customization;

20 Indian monsoon region

22 **Abstract.** Mitigation of carbonaceous aerosol emissions is expected to provide climate and

23 health co-benefits. The accurate representation of carbonaceous aerosols in climate models is

24 critical for reducing uncertainties in their climate feedback. In this regard, emission fluxes and

25 aerosol life-cycle processes are the two primary sources of uncertainties. Here we demonstrate

26 that incorporating a dynamic ageing scheme and emission estimates that are updated for the

27 local sources improve the representation of carbonaceous aerosols over the Indian monsoon

28 region in a regional climate model, RegCM, compared to its default configuration. The mean

29 BC and OC surface concentrations in 2010 are estimated to be 4.25 and 10.35 μg m^{-3},

30 respectively, over the Indo-Gangetic Plain (IGP), in the augmented model. The BC column

31 burden over the polluted IGP is found to be 2.47 mg m^{-2}, 69.95 % higher than in the default

32 model configuration and much closer to available observations. The anthropogenic AOD

33 increases by more than 19 % over the IGP due to the model enhancement, also leading to a

34 better agreement with observed AOD. The top-of-the-atmosphere, surface, and atmospheric

35 anthropogenic aerosol shortwave radiative forcing are estimated at -0.3, -9.3, and 9.0 W m^{-2},

36 respectively, over the IGP and -0.89, -5.33, and 4.44 W m^{-2}, respectively, over Peninsular India

37 (PI). Our results suggest that both accurate estimates of emission fluxes and a better

38 representation of aerosol processes are required to improve the aerosol life cycle representation

39 in the climate model.

40

1. Introduction

42   Carbonaceous aerosols (organic carbon, OC, and black carbon, BC) emitted from

43 incomplete combustion constitute 20%-50% of the total global aerosol mass (Kanakidou et al.,

44 2005; Putaud et al., 2010), causing substantial air quality degradation (Singh et al., 2021). Due

45 to their ability to absorb solar radiation, carbonaceous aerosols also contribute to global

46 warming (Ramanathan and Carmichael, 2008). Hence, they are considered to be key short-

47 lived climate pollutants (SLCPs) (UNFCC, 2015), and mitigating their emissions is expected

48 to result in both climate and health co-benefits (Tibrewal and Venkataraman, 2021; Naik et al.,

49 2021). Climate models are characterized by large discrepancies in simulating carbonaceous

50 aerosol loadings, their optical properties, and radiative forcing (Ajay et al., 2019), primarily

51 due to uncertainties in emission inventories and limitations in the treatment of aerosol processes

52 in the models (Bond et al., 2013). Unless the representation of the life cycle of carbonaceous

53 aerosols in climate models is improved, their role in climate impacts and air quality degradation

54 cannot be assessed accurately (Riemer et al., 2019).

55   A multi-institutional network program - Carbonaceous aerosol emissions, source

56 apportionment, and climate impacts (COALESCE) was launched by the Government of India

57 to address some of these issues for the Indian monsoon region (Venkataraman et al., 2020).

58 One of the scientific objectives of COALESCE is to understand and reduce uncertainties in

59 representing carbonaceous aerosol life cycle in global and regional climate models, focusing

60 on the Indian subcontinent. The regional climate model, RegCM4, developed at the

61 International Centre for Theoretical Physics (ICTP), Italy (Giorgi et al., 2012), is one of the

62 participating models in COALESCE. RegCM4 was extensively used to examine variability in

63 the Indian summer monsoon (Dash et al., 2015; Rai et al., 2020), to project climate change over

64 South Asia (Pattnayak et al., 2018), and to elucidate the dynamical impacts of aerosols on the

65 Indian summer monsoon in the present (Das et al., 2015, 2016) and future (Das et al., 2020)

66 climate conditions.

The aerosol module in the RegCM4 (Solmon et al., 2006; Zakey et al., 2006) considers various aerosol life cycle processes, such as emission (source), advection, horizontal and vertical diffusion, transport, conversion of hydrophobic to hygroscopic species and wet and dry deposition (sink) (see Methods for more details). Previous studies (Das et al., 2016; Nair et al., 2012) have pointed out that the RegCM4 underestimates the anthropogenic aerosol loading over the Indian subcontinent, and therefore, the net aerosol impact over the region is dominated by natural aerosols (Das et al., 2020). We recently implemented a dynamic ageing scheme in the RegCM aerosol module (Ghosh et al., 2021), which converts carbonaceous aerosols from hydrophobic to hygroscopic states based on the aerosol number concentration. Compared to the constant conversion rate of 27.6 hours used in the default version of the model, the scheme allowed a faster conversion in the polluted regions than in the clean areas of the South Asia region. This, in turn, affected the aerosol forcing due to the changes in aerosol loadings induced by the new hydrophobic-to-hygroscopic conversion scheme. It was also found that implementing the dynamic ageing scheme alone is not sufficient to fully improve the model performance and hypothesized that much of the model uncertainty was due to the emission inventory.

In this work, we examined the changes in carbonaceous aerosol burden and their impact on the radiation budget of the South Asia region due to the combined impact of the improved dynamic ageing scheme and a regional emission inventory (Pandey and Venkataraman, 2014; Sadavarte and Venkataraman, 2014) replacing the global emission inventory used in the default model version (see Methods). We carried out four sets of simulations for the year 2010 - (1) control simulation with the default (fixed) ageing scheme and global inventory (hereafter Default_Sc), (2) simulation with the dynamic ageing scheme and global inventory (Dyn_global), (3) simulation with the default ageing scheme and regional inventory (Fix_Regio) and (4) simulation with the dynamic ageing scheme and regional emission inventory (Dyn_Regio). The changes due to ageing alone (i.e., Default_Sc vs. Dyn_global) have already been reported in Ghosh et al. (2021). Here we analyse and report the improvements in model performance due to the combined impact of incorporating a better emission inventory and a more realistic ageing scheme relative to the default model configuration (i.e., Default_Sc vs. Dyn_regio) and investigate these performance changes in terms of the aerosol processes considered in the model. However, the changes due to emission alone (i.e., Default_Sc vs. Fix_regio) will be considered as an intermediate step towards Dyn_regio.

2. Data and Methodology

2.1 Model configuration

RegCM version 4 is a hydrostatic, compressible, primitive equation and sigma-p vertical coordinate model with a dynamical core from the NCAR Mesoscale Model Version 5 (MM5) (Grell et al., 1994). We have used the Community Climate Model Version 3 (CCM3) (Kiehl et al., 1996) radiative transfer scheme with the modifications described in the literature (Giorgi et al., 2012). The model is interactively coupled with both natural (dust and sea salt) (Zakey et al., 2006, 2008) and anthropogenic aerosols (Solmon et al., 2006), along with a gas-phase chemistry module (Shalaby et al., 2012), but for this study, we have only considered the anthropogenic module (Solmon et al., 2006). The choice of parameterisation schemes for our experiments has been provided in the following table:

Land surface processes	Biosphere-Atmosphere Transfer Scheme (BATS) (Dickinson et al., 1993)
Planetary boundary layer	University of Washington (UW) scheme (Grenier and Bretherton, 2001; Bretherton et al., 2004; O'Brien et al., 2012)
Cumulus convection scheme	Emanuel (Emanuel and Živković-Rothman, 1999) over land and Tiedtke (Tiedtke, 1993) over the ocean
Large-scale cloud and moisture process	SUBEX scheme (Pal et al., 2007, 2000)
Aerosol module	SUCA (Solmon et al., 2006)
Emission inventories	IIASA and IIT Bombay 2010

The anthropogenic aerosol module consists of sulphate, hydrophilic and hydrophobic BC, and hydrophilic and hydrophobic OC, along with a sulphate scheme (Qian et al., 2001). The mass concentrations of these species are tracked, assuming that they form an external mixture. The emitted carbonaceous aerosols are considered to be 80 % hydrophobic and 20 % hydrophilic for BC, while equal fractions of hydrophobic and hydrophilic OC are considered in the simulations. The rate of change of mass mixing ratios of hydrophobic and hydrophilic tracers, indicated by subscript 'hb' and 'hl,' is described by the chemical transport equation in Solmon et al. (2006).

The atmospheric lifetime of aerosols is governed by dry and wet deposition. The dry deposition velocity depends on the type of surface, while the dry deposition flux variation is

proportional to the tracer concentration in the lowest level of the model (around 30 m above the surface). Wet deposition in the RegCM4 has been split into "in-cloud" and "below-cloud" terms. The in-cloud removal process starts for large-scale clouds if the liquid water is higher than the threshold level (0.01 g m^{-3}) in the model layers where the cloud fraction is more than zero and is a function of the fractional removal rate of liquid water (fraction of precipitating rain over liquid water content of the atmospheric layer, the in-cloud removal rate for cumulus clouds is constant and fixed at 0.001 s^{-1}) and the aerosol solubility. This solubility is different for different species, and thus hydrophilic and hydrophobic BC/OC have different in-cloud wet deposition rates. The below-cloud washing out of the aerosols is controlled by their effective diameters and densities. Collection efficiency for each aerosol species is computed from the aerosol effective diameter and density, which is different for different species. The changes in wet and dry deposition alter the ratio of hydrophobic to hydrophilic changes, which in turn alters the atmospheric lifetime of aerosols. A detailed explanation regarding these changes due to ageing alone can be referred to Ghosh et al. (2021). Seasonal variation in the lifetime of particles, at the surface and upper atmosphere, due to ageing alone has been already explained in Ghosh et al. (2021).

The model was simulated over the South-Asian CORDEX domain (Giorgi et al., 2009) [20° S - 50° N and 10°-130° E] for the year 2010 at 0.25° × 0.25° resolution, while the results are analysed over the Indian subcontinent [0°-45° N and 60°-105° E] with special focus on the IGP [25°-30° N and 73°-89° E] and PI [8°-20° N and 72°-85° E]. The model consists of 18 vertical levels with 50hPa as the model top pressure. There are three levels (1000, 925, 850 hPa) within the boundary layer. ERA-Interim reanalysis dataset, at 1.5° resolution and 6-hourly temporal resolution, has been used to generate the initial and lateral meteorological boundary conditions for the study (Dee et al., 2011). The sea surface temperature was derived from the NOAA Optimum Interpolated weekly 1° × 1° gridded data and the chemical boundary conditions from MOZART 6-hourly data. Four sets of simulations have been performed for the year 2010 - (1) control simulation with the default (fixed) ageing scheme and global inventory (hereafter Default_Sc), (2) simulation with the dynamic ageing scheme and global inventory (Dyn_global), (3) simulation with the default ageing scheme and regional inventory (Fix_Regio) and (4) simulation with the dynamic ageing scheme and regional emission inventory (Dyn_Regio). In each of the experiments, the model was simulated from October 01, 2009, to December 31, 2010. The first three months were considered spin-up and thus were not included in the analysis. The focus of this manuscript is the Indian landmass only. Changes in

aerosol properties over the oceans have not been discussed because the oceanic condition is mostly clean with low tracer concentration compared to that over the landmass. In the supplementary material Fig S1, there are hardly any emissions over the oceans. Additionally, in (Ghosh et al., 2021), it is evident that the ageing time of the carbonaceous aerosols over the oceans is larger than the default ageing timescale.

2.2 Emission inventories

In this study, we considered a global emission inventory [https://www.iiasa.ac.at/web/home/research/researchPrograms/air/Global_emissions.html] and a regional emission inventory (Pandey and Venkataraman, 2014; Sadavarte and Venkataraman, 2014; Venkataraman, 2018). Figure S2 represents the seasonal variation of the emissions estimated by the two inventories. The global emission inventory used in the experiments 'Default_Sc' and 'Dyn_global' was developed by the IIASA emission inventory at a resolution of $0.5° \times 0.5°$ [https://www.iiasa.ac.at/web/home/research/researchPrograms/air/Global_emissions.html]. The key emission sectors considered in this inventory are energy, industry, solvent use, transport, domestic combustion, agriculture, open burning of agricultural waste, and waste treatment. The emission estimates were available only at an annual scale with no seasonal variation from 1990-2010.

The regional emission inventory used in experiments 'Fix_regio' and 'Dyn_regio' was developed by IIT Bombay (Pandey and Venkataraman, 2014; Sadavarte and Venkataraman, 2014; Venkataraman et al., 2018) at a horizontal resolution of $0.25° \times 0.25°$ and the estimates vary at a monthly scale. Thus, the regional emissions have a profound seasonal variability (Figure S1). The key sectors included in the regional inventory are energy (coal + oil + gas), heavy and light industry, brick production, residential cooking, solid biomass fuel, residential cooking (LPG and kerosene), residential lighting (kerosene lamp), residential water heating, residential space heating, informal industry, agricultural residue burning, on-road gasoline, on-road diesel, railway, agricultural diesel pump, agricultural tractors. Among these sectors, residential water heating, residential space heating, and agricultural residue burning sectors have seasonality in emissions.

2.3 In-situ BC data

188   In-situ BC data for the year 2010 has been procured from 24 sites to evaluate the model

189   performance. These sites have been shown in the supplementary Fig S4. 21 of these sites are

190   part of the Indian Space Research Organization's Aerosol Radiative Forcing over India

191   Network, ARFINET (Babu et al., 2013; Gogoi et al., 2021). This network has been measuring

192   columnar AOD and BC for many years. In addition to the ARFINET, BC concentrations are

193   also measured independently at Kanpur (Tripathi et al., 2005) (entire 2010 except during the

194   monsoon season), Gadanki (Gadhavi et al., 2015; Jain et al., 2018), and Delhi (October-

195   December 2010) by individual institutions. In all the sites, BC was measured by an

196   Aethalometer. An aethalometer measures the amount of attenuation of the light beam passing

197   through the filter where particles get deposited. BC mass concentration is measured by the

198   change in optical attenuation given by the rate of BC deposition on the filter tape (Hansen et

199   al., 1984). Dataset from all the sites except Gadanki (monthly values) are available on a daily

200   scale and have been averaged to get the annual concentrations.

201

202   **2.4 MERRA-2 data**

203   Model simulated BC and OC columnar burdens have been evaluated against MERRA-2

204   reanalysis data. MERRA-2 is an updated reanalysis of atmospheric data produced by the NASA

205   Global Modeling and Assimilation Office (Buchard et al., 2017). MERRA-2 consists of

206   parameters that are not available in its predecessor, MERRA. It includes updates of the

207   Goddard Earth Observing System model and analysis scheme in order to give a more realistic

208   view of the ongoing climate analysis beyond MERRA's jargon. This dataset addressed the

209   limitations of MERRA. Various improvements in MERRA-2 include assimilation of aerosol

210   observations and improved representation of stratosphere, including ozone and cryosphere.

211   MERRA-2 data products are freely accessible through the NASA Goddard Earth Sciences Data

212   Information Services Center. We note that MERRA-2 data are also not observations and direct

213   validation of the MERRA-2 columnar BC and OC burden is not possible.

214

215   **2.5 MISR aerosol data**

216   MISR on-board Terra satellite crosses the equator around 10:30 hrs local time. It has a high

217   spatial resolution and a wide range of viewing angles. It views the Earth using four spectral

218   bands in each of the nine cameras and has a weekly global coverage between ±82º. A detailed

219   description is provided in the literature (Diner et al., 1998). MISR-AOD has a correlation

220   coefficient of ~0.9 (for maritime sites) and ~0.7 (for dusty sites) w.r.t AERONET (Kahn et al.,

221 2005). In the absence of any direct measurement of anthropogenic AOD, we use MISR fine
222 AOD (AOD for particles smaller than 0.35 μm) (Dey and Di Girolamo, 2010).

223

3. Results

In this section, we have discussed the three-dimensional annual distribution of carbonaceous aerosols (sections 3.1 and 3.2) for the default (Default_Sc) and augmented (Dyn_regio) model set-up. The seasonal distributions for all four experiments – Default_Sc, Dyn_global, Fix_regio, and Dyn_Regio, have been reported in the supplementary information (SI). In section 3.3, we have investigated the annual changes in aerosol optical properties due to the default (Default_Sc) and augmented (Dyn_regio) model set-up. In this case, also, the seasonal variability across the four experiments has been shown in the SI.

3.1 Spatial distribution of carbonaceous aerosols

Figure 1 shows the spatial distributions of the annual surface concentration for BC and OC using the default and augmented model, along with their differences. Several key features are notable. First, the OC concentration is almost three times higher than the BC concentration in the augmented model, consistent with the literature (Priyadharshini et al., 2019). Secondly, the concentrations are 2-3 times higher over the polluted Indo-Gangetic Plain (IGP) compared to the rest of India in the augmented model. High aerosol loadings in the IGP are a result of the combined effects of greater source strength, low topography surrounded by highlands to the north and south, and unfavourable meteorology (Dey and Di Girolamo, 2010; Srivastava et al., 2012). Thirdly, the BC and OC concentrations increase by >100 % and >60 %, respectively, over the IGP and by smaller margins elsewhere in the augmented model relative to the default configuration. The increase in the annual tracer concentrations can be further explained by the seasonal distributions and the selected model configuration. To begin with, an increase in both BC and OC concentrations during the winter (JF), pre-monsoon (MAM), and post-monsoon (OND) seasons are clearly visible in Fig S2 and Fig S3 (see Supplementary Information SI). During the monsoon, precipitation removes large amounts of aerosols; as a result, the increase in BC concentration is almost negligible, and for OC, it is negative. The transition in concentration from Dyn_global to Fix_regio is most prominent than that from Default_Sc to Dyn_global or Fix_regio to Dyn_regio. This indicates the impact of the switch from the global to regional emission inventory (Figure S1) is greater than the impact of the implementation of the dynamic ageing scheme (Figure S1) on the increases in BC and OC mass concentrations in the augmented model.

254
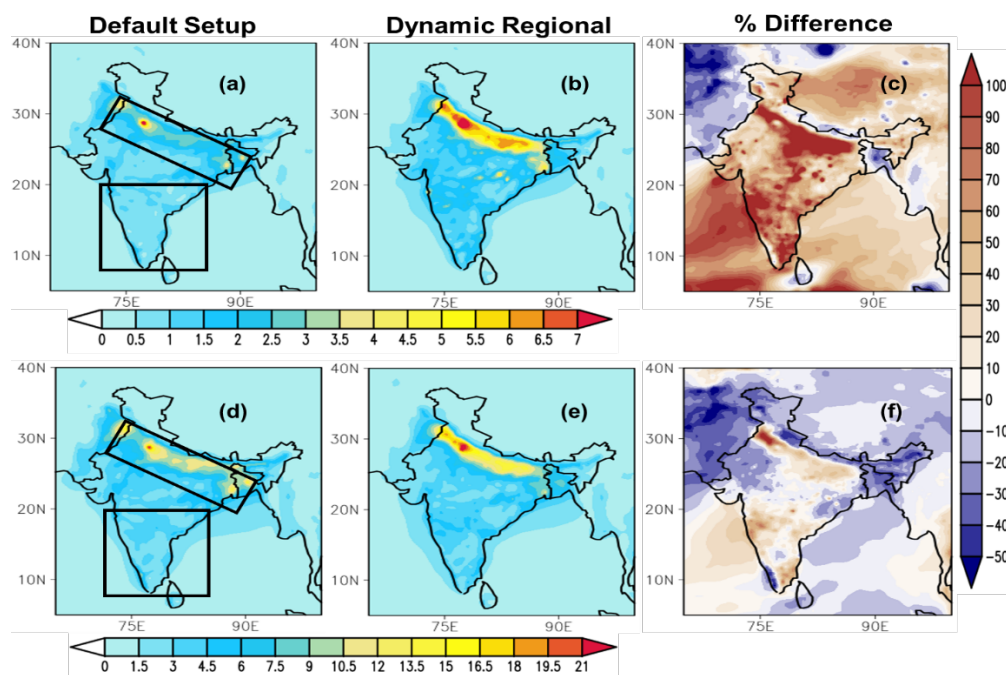
255

256

257   **Figure 1** Spatial distribution of surface mass concentration ($\mu g\ m^{-3}$) of BC (a, b) and OC (d, e)

258   in 2010 over the Indian subcontinent using (left) the default and (middle) the augmented model

259   configurations. Figures 1c and 1f represent the corresponding percentage differences due to the

260   augmented model set-up (positive values imply an increase in mass concentration). The vertical

261   distributions (shown in Figure 3) are analysed for the IGP and PI sub-regions marked by boxes

262   in the panels of the left column.

263

264   We evaluate the performance of the customized model against BC surface concentrations

265   measured at 24 sites across India (Figure 2). We note that the in-situ concentrations are point

266   measurements, while the model grids containing these sites are representative of 25 km by 25

267   km areas. The default model severely underestimates the surface BC compared to the in-situ

268   observations (mean normalized bias, MNB = -69 %). Though the underestimation persists in

269   the augmented model (by varying proportions across the sites), the simulated concentration

270   magnitudes are closer to the observations (MNB = -51 %), particularly in the mega-cities of

271   the polluted IGP (e.g., Delhi, Kanpur, Varanasi, Kharagpur). The improvement is small in some

272   cities, particularly in the East India region (e.g., Dehradun, Dibrugarh, Ahmedabad), where the

273   differences in global and regional emission inventories are also small. This suggests that the

274   problem could be related to the emission fluxes. In several cities, especially in the North and
275   South Indian regions (e.g., Goa, Nainital, Ooty, Thiruvananthapuram), the simulated BC using
276   the augmented model is a very close match with the observations. Overall, the augmented
277   model ($R^2 = 0.66$) performs better than the default model ($R^2 = 0.6$) in simulating surface BC
278   concentrations, and the errors shown in Figure 2 could also be amplified by the fact that the
279   model data refers to a 25 km $\times$ 25 km area as a single grid.

280
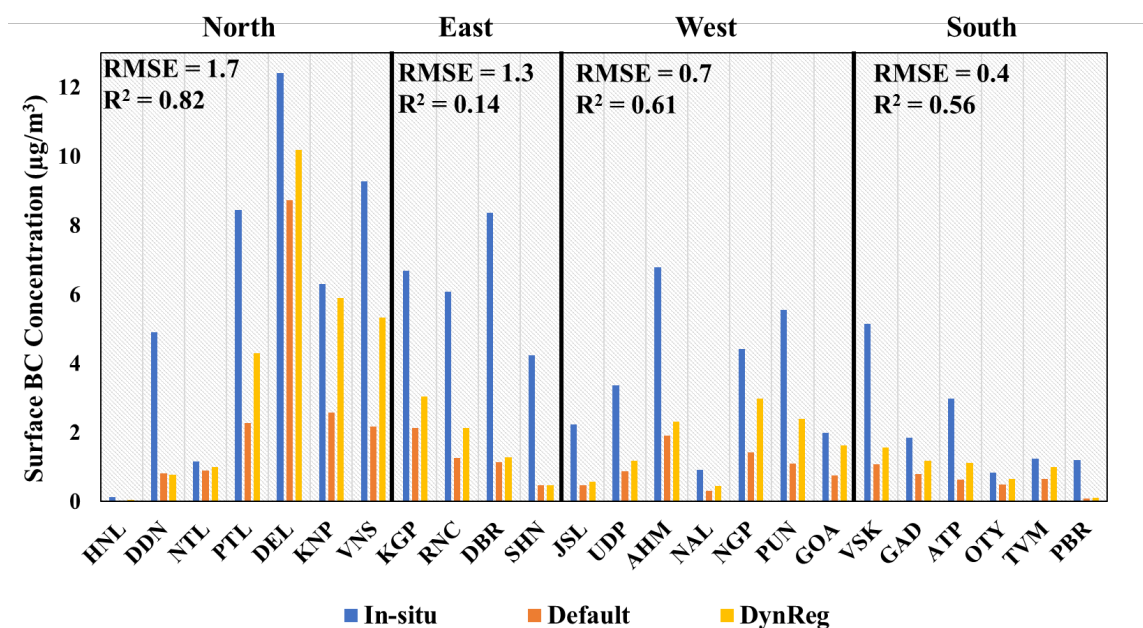
281

282

283   **Figure 2** Comparison of simulated BC surface concentration (μg m^{-3}) using the default and
284   augmented model with in-situ measurements from 24 cities across India. Locations of the cities
285   are shown in Figure S4. RMSE (in μg m^{-3}) and R^2 between the customized model simulations
286   and surface measurements are also provided.

287

288   Since there are no in-situ measurements of columnar burden, we compare the simulated
289   columnar burden (Figure 3) with data from Modern-Era Retrospective Analysis for Research
290   and Applications, version 2 (MERRA-2) (Buchard et al., 2017). Similar to the surface mass
291   concentration, the BC burden shows a more pronounced change than the OC burden due to the
292   inclusion of the new model features. Here also, the introduction of the emissions alone played
293   a more prominent role than the dynamic ageing alone (see Figure S5 and Figure S6 in SI), but
294   the highest change can be observed in the presence of both. Though the simulated burden is

still underestimated relative to the MERRA-2 data, the values in the augmented model are much closer to the reanalysis data, and the sequence of changes (in both BC and OC) follow Dyn_regio > Fix_regio > Dyn_global > Default_sc. During the winter season (Jan-Feb), the percentage difference of model-simulated column burden (w.r.t. MERRA-2) decreases from >70 % to ~ 35 % for BC and from ~63 % to ~49 % for OC in the augmented model (Figure S5 and S6). A similar improvement is found in the pre-monsoon season (Mar-May). The higher BC loading over the IGP results from higher magnitudes of regional emissions coupled with faster ageing and slower removal rate. The percentage difference increases for OC burden over northwest India decreases over the IGP and is negligible over the rest of the country. A probable explanation for such OC distribution relies on the emission inventories used since the OC emissions are slightly higher in the global inventory than those in the regional inventory over northwest India and lower in the IGP. Emissions over the PI are roughly similar in the two inventories (Figure S1). The role of emissions in both BC and OC simulated burden is further supported by the observed transition changes from Dyn_global to Fix_regio. We also note that anthropogenic aerosol emissions vary on an annual basis in MERRA-2 (Buchard et al., 2017); hence, there could be larger uncertainties at a seasonal scale.

During the monsoon season (Jun-Sep), the BC loading increases, and OC loading decreases in magnitude in the augmented model compared to the default set-up (Figure S5), mostly due to the implementation of the regional inventory. The magnitude of the simulated BC column burden is comparable between the Default_Sc and Dyn_sc experiments and that between the Fix_Regio and Dyn_Regio (Figure S5), with an opposite pattern found for the OC column burden (Figure S6). Two possible reasons can explain this result. First, the OC emissions in the global inventory are higher than in the regional ones (Figure S1). Second, the model assumes that OC is 50 % hydrophobic and 50 % hydrophilic at the time of emission (for BC, it is 80 % hydrophobic and 20 % hydrophilic), and therefore the faster conversion to hydrophilic OC due to the dynamic ageing can enhance the hydrophilic OC removal by rain. On analysing the wet removal (refer to Figure S7 and Figure S8 in SI), BC_HL showed the expected highest removal during JJAS, but OC_HL showed a lower magnitude of wet removal. Therefore, lower OC emissions in the regional inventory play a major role, during JJAS, in simulating OC burden in the augmented model. In the post-monsoon season (Oct-Dec), an overall increase in column burden in the augmented model is observed throughout India. Higher emissions (in the case of the regional inventory) result in higher concentrations of available condensing and coagulating particles, which in turn allows faster ageing of hydrophobic to hydrophilic BC leading to

328 accumulation of BC particles in the atmosphere before their removal by dry deposition. The

329 changes in the OC loading are negligible in this season (refer to Figure S6 in SI).
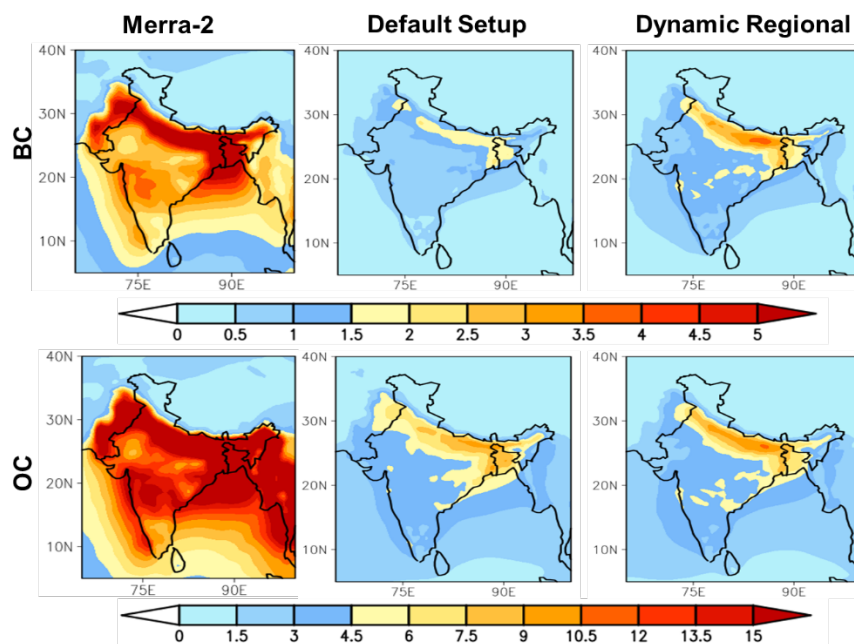
330

331 **Figure 3** Comparison of spatial patterns of annual (top panel) BC and (bottom panel) OC

332 column burden (mg m^{-2}).

333

3.2 Vertical distribution of carbonaceous aerosols

335 In this section, we analyse the effects of the model improvements on the vertical

336 distribution of aerosols over the IGP and compare the results with the contrasting PI region,

337 where the emissions are much lower. The two regions are indicated by the boxes in Figure 1.

338 Figure 4 represents longitude-altitude cross-sections of annual BC and OC mass concentration

339 (μg m^{-3}) over the regions. The vertically distributed mass concentrations (μg m^{-3}) of both BC

340 and OC increase due to the model improvements up to 500 hPa. Similar to spatial distribution,

341 here also seasonal variability will help to explain the annual vertical concentrations.

342 Furthermore, the changes are more dramatic and prominent over IGP than that over PI.

343
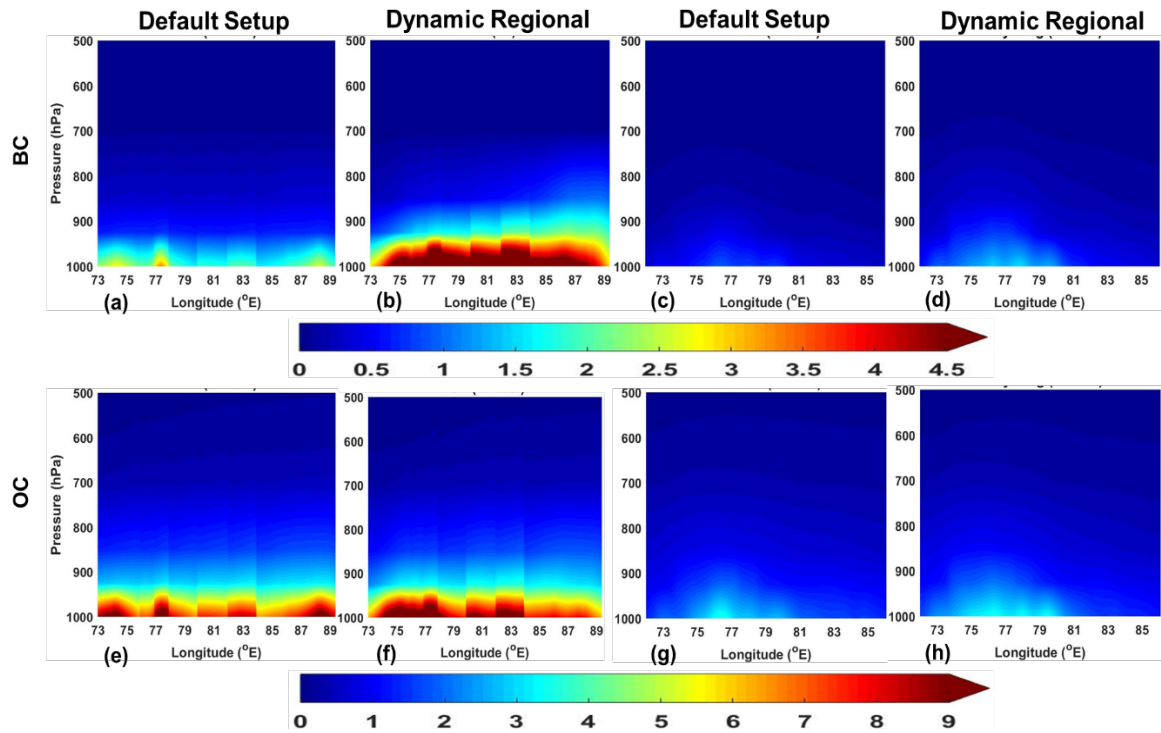
Figure 4 Longitude (in °E)-altitude (in hPa) cross-sections of (top panel) BC and (bottom panel) OC mass concentration (µg m^{-3}) over the IGP (a, b, e, f) and PI (c, d, g, h) for the default and customized model.

Over IGP, a larger increase is observed during the winter and post-monsoon seasons (Figures S9 and S10). Both the BC and OC concentrations (µg m^{-3}) are comparable in the default and Dyn_global configurations, but they increase in the Fix_regio and Dyn_regio set-ups (Figures S9 and S10). In these two seasons, both BC and the OC are distributed up to the mid-tropospheric levels but with differing magnitudes. This is indicative of higher concentrations of OC vertical transport than that of BC. During the pre-monsoon season, the vertical distributions of both BC and OC show responses similar to that of their spatial distributions. In the monsoon season, the tracer concentration is mainly confined to the surface levels, indicating a lower wet removal and slower ageing above 1000 hPa (Ghosh et al., 2021). For further clarification of the seasonality of the vertical pumping effect, the convective tendency (represents vertical transport) and lateral advection (represents horizontal transport) have been investigated. The model simulated convective tendency and lateral advection (responsible for long-range transport) are given below. More positive values indicate a strong updraft above the surface due to convection. Convection tendency gradually increases from left to right (Figure 5 for BC and Figure S11 in SI for OC). Particularly in the drier seasons

since more particles are available in the absence of washout. During winter, the augmented model (Dyn_regio) shows a lesser pumping effect over IGP than that when only emissions have been changed (Fix_regio). This can be due to the fact that in the presence of dynamic ageing a greater number of hydrophilic tracers are available for removal (evident from the removal plot of BC_HL) even for a small amount of precipitation from western disturbances. However, during post-monsoon (OND), due to negligible precipitation over IGP, removal rates of hydrophilic tracers are comparable, and hence the pumping effect also follows the same trend. A similar trend in convective tendency is also shown by OC particles (Figure S11 in SI). The magnitude of OC convection tendency is stronger than that of BC particles, probably due to a higher concentration (Priyadharshini et al., 2019; Ram et al., 2010) of available particles. Besides, lateral advection is an indicator of horizontal long-range aerosol transport. More positive values indicate strong flow along the surface due to advection. Advection shows strong seasonality (from top to bottom – Figure 6 for BC and Figure S12 in SI for OC). In drier months (JF and OND), horizontal transport is comparatively less than in pre-monsoon (MAM) and monsoon (JJAS). Therefore, vertical convection is more prominent in dry seasons while horizontal advection is dominant for MAM and JJAS, irrespective of the choice of schemes. Consequently, the observed BC concentration is due to convection in JF and OND and due to advection in MAM and JJAS. Similar logic can be applied for OC concentration distribution due to lateral advection (Figure S12 in SI). However, the positive advection signal is stronger than that of BC particles. This can be again due to the higher concentration of available particles for transport to other regions.

In addition, the atmospheric profiles over the region have also been used to explain the tracer distribution. In terms of changes in temperature profile, higher temperatures over IGP during MAM and JJAS facilitated the strong vertical wind movement (negative values in Figure S13). But negative convective tendency (Figure 5 for BC and Figure S24 in SI for OC) and positive lateral advection of (Figure 6 for BC and Figure S23 in SI for OC) carbonaceous aerosols during these months lowered their concentrations. This is further supported by the high RH values particularly in JJAS (Figure S14) which resulted in higher removal. Exactly opposite is happening during the drier months (JF and OND). Comparatively low temperatures (Figure S15), facilitated more stable wind movement (positive values in Figure S13). However, in presence of high emissions, the aerosol pumping effect resulted in strong convective tendency (Figure 5) which further facilitated the higher concentrations during these months. The low RH values (Figure SX2) during these months are also conducive of higher aerosol atmospheric lifetime.

399
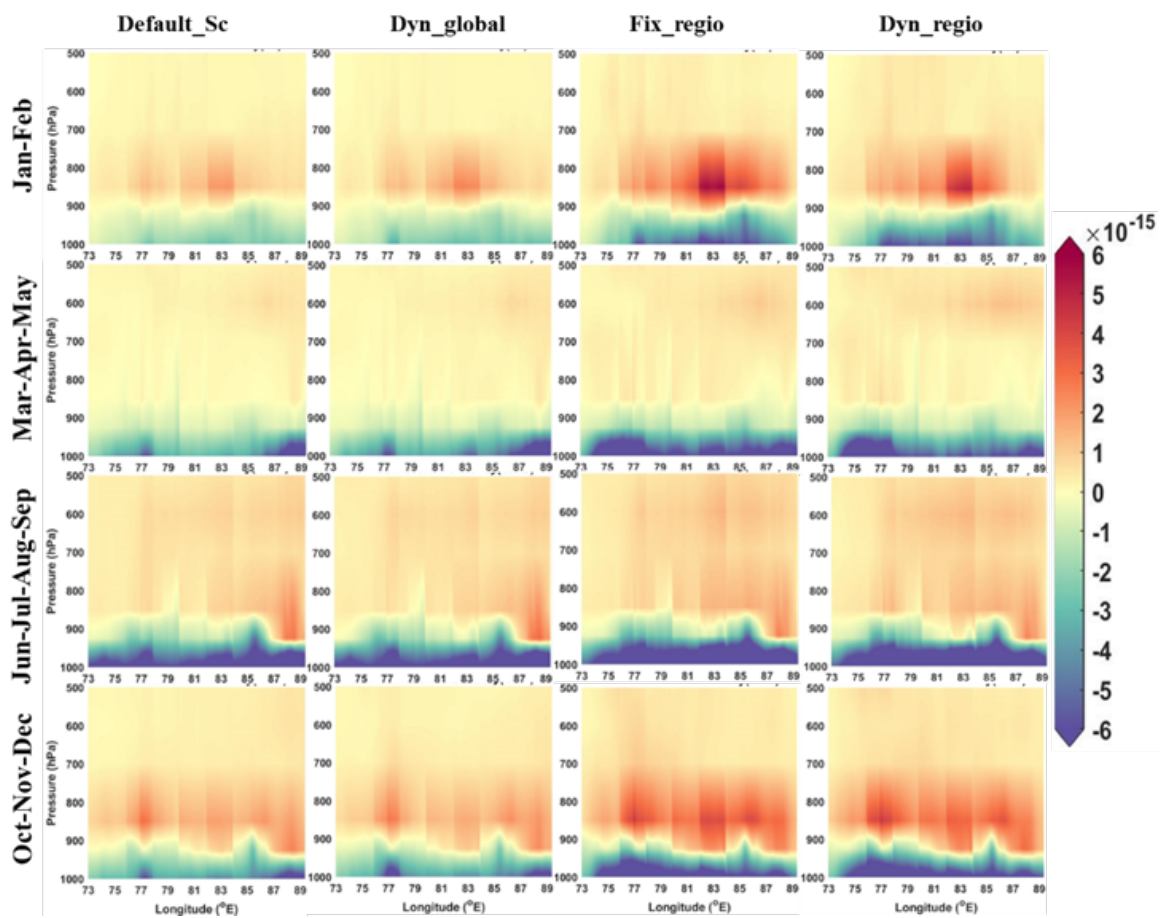
Figure 5 Seasonal distribution of convective tendency (kg kg^{-1} s^{-1}) of BC over IGP for four distinct experiments.
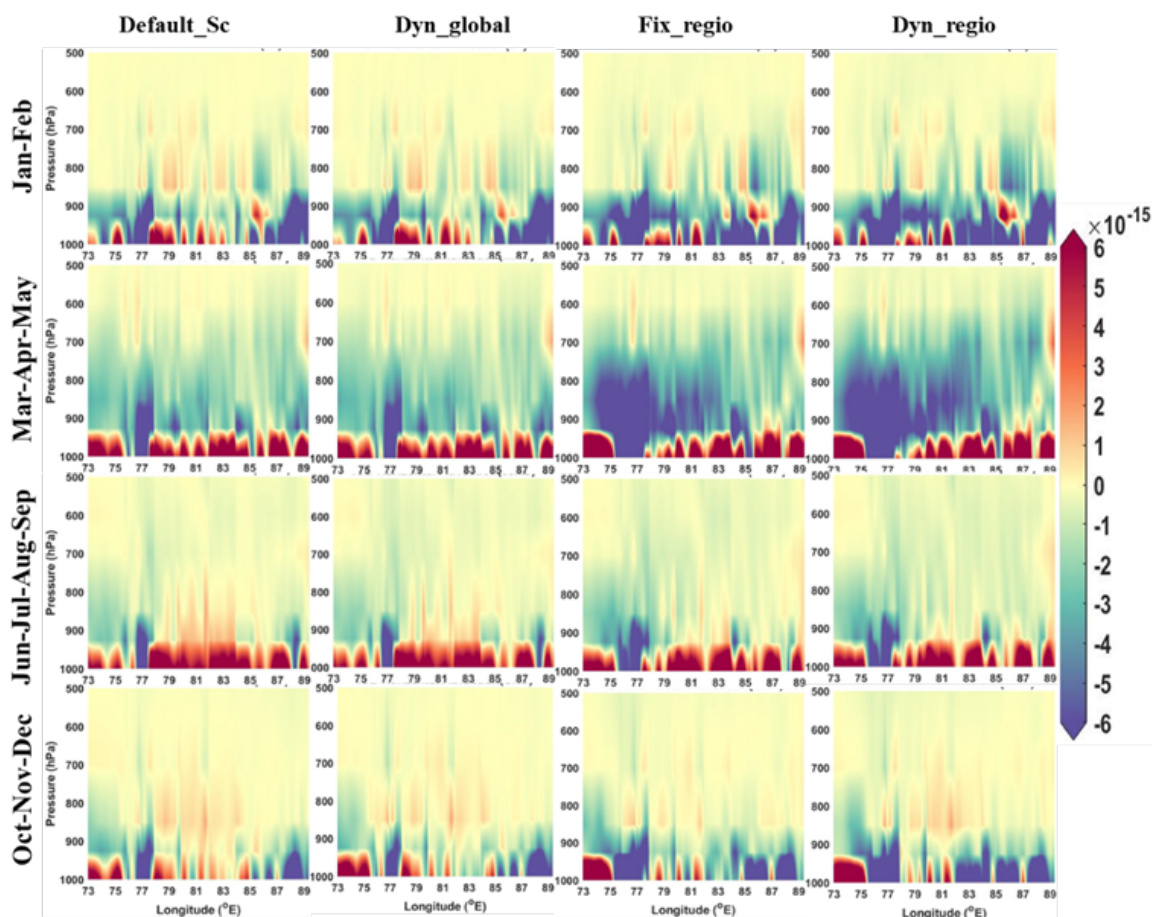
Figure 6 Seasonal distribution of lateral advection (kg kg^{-1} s^{-1}) of BC over IGP for four distinct experiments.

Over the PI, the annual concentrations of carbonaceous aerosols (Figure 4) are very low than over the IGP, which limits the impact of dynamic ageing because of the lower availability of condensing and coagulating particles (relative to the IGP). This results in a slower ageing and lower accumulation of hydrophilic tracers in the troposphere. However, the vertical pumping effect is quite prominent during the winter season in the augmented configuration (Figures S16 and S17). During the pre-monsoon season, only the BC concentration shows an increment in the lower troposphere, while the OC concentration remains more or less unchanged. The PI receives rainfall during the southwest and northeast monsoon; hence the tracer concentration is further lowered during the monsoon and post-monsoon seasons. This is further supported by the high relative humidity values over PI during monsoon and post-monsoon (Figure S18). The high humidity during JJAS can also influence a comparatively high, near surface air temperature (Figure S19) by trapping the radiation. This in turn resulted

422 in a high vertical wind shear (Figure S20) over PI during this season. But the convective
423 tendency is low for both BC and OC (Figure S21 and S24 respectively).

424 The lower concentration can be, therefore, primarily because of the lower emissions for both
425 BC and OC (refer to Figure S1). This argument is further supported by lower washout than IGP
426 (Figure S7 and S8) in spite of high RH values (Figure S24). Since, the convective tendency, as
427 well as lateral advection for BC, is not playing any major role (as can be seen in Figure S21
428 and Figure S22 in SI), therefore again concluding the role of lower emissions. In the case of
429 OC, lateral advection (Figure S23 in SI) and comparatively lower emissions (Figure S1 in SI)
430 than IGP can be the predominant factors for lower concentration over PI in the presence of
431 negative convective tendency (Figure S24 in SI).

432

433 **3.3 Optical and radiative properties of anthropogenic aerosols**

434 We now examine the effects of the model improvements on the optical properties of
435 anthropogenic aerosols. In this regard, we note that the changes due to the implementation of
436 the dynamic ageing scheme can alter only BC and OC concentrations, while the changes related
437 to the emission inventory impact the sulphate concentration as well. We consider the AOD due
438 to small particles (radius<0.35 μm) from the Multiangle Imaging Spectroradiometer, MISR
439 (Kahn and Gaitley, 2015), as a proxy for anthropogenic AOD (hereafter AAOD) since direct
440 measurement of AAOD are not available to evaluate our model performance (Figure 7).

441 The simulated annual AAOD is >50 % lower than the MISR small-AOD over the polluted
442 IGP and 30-50 % lower over the PI in the default model. This is consistent with the previous
443 studies (Nair et al., 2012). These model underestimations improve by 25-35 % over the IGP
444 and parts of PI in the augmented model. The seasonal plots (Figure S8) clearly show an increase
445 in AAOD in all seasons except during the monsoon. This increase in AAOD is due to both the
446 implementation of region-specific emission fluxes (Nair et al., 2012) and the dynamic ageing
447 scheme (Ghosh et al., 2021). The AAOD still remains underestimated in some regions, which
448 can possibly be addressed by further improvements of the emission estimates, for example, the
449 addition of missing sectors (e.g., crematorium, municipal solid waste burning, etc.), improving
450 sectoral methodologies for informal activities and incorporation of regionally measured
451 emission factors.

452

453
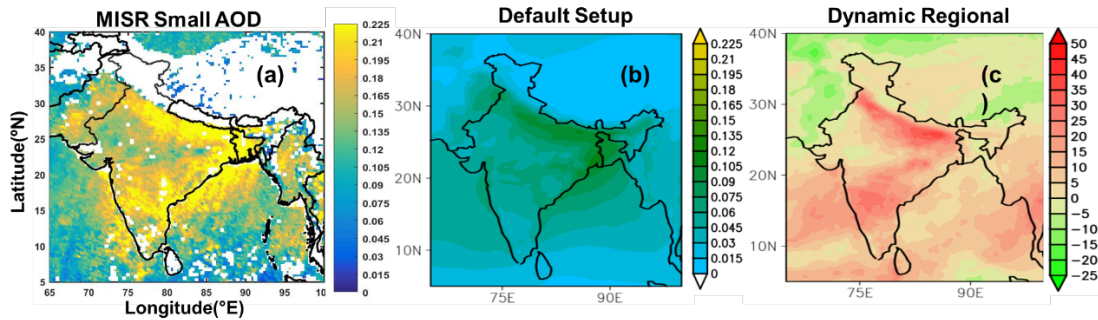
Figure 7 Spatial distribution of (a) MISR small mode AOD ('white' color implies 'no data'), (b) AAOD simulated by default_sc, and (c) percentage increase in AAOD simulated by the augmented model w.r.t default_sc for 2010.

Spatial patterns of the annual top-of-the-atmosphere (TOA), surface, and atmospheric radiative forcing associated with the anthropogenic aerosols for the augmented model are shown in Figure 8. Currently, the model does not assume aerosol interaction with clouds; therefore, the radiative feedback is mainly governed by direct radiative forcing. Hence, secondary effects due to aerosols cannot be considered for the observed values in Fig 8. The TOA aerosol radiative forcing lies in the range of -0.5 to -1.5 W m^{-2} over most of the Indian landmass, except the IGP, where it is positive (0.25 to 1 W m^{-2}) due to the higher concentration of carbonaceous aerosols (Figure 1 and Figure 3), particularly BC. The TOA forcing is also positive over the Indian desert and snow-covered regions even when the carbonaceous aerosol concentrations are lower or comparable to the rest of India. The high surface albedo in these regions allows for an enhanced interaction of the carbonaceous aerosols with solar radiation, resulting in a warming effect (Satheesh, 2002). The surface radiative forcing is found to be larger than -10 W m^{-2} over the polluted IGP, which is consistent with published results (Ramanathan and Carmichael, 2008). Over the rest of India, the surface forcing values lie between -3 to -8 W m^{-2}. Due to the model improvements (forcing estimates with the default model are shown in Figure 8), the TOA forcing changes by -72.75 %, and the surface dimming increases by 39.73 % over the IGP and by -23.94 % and 34.35 %, respectively, over PI. As a result, the atmospheric heating increases by ~9 W m^{-2} over the IGP. The simulated surface shortwave radiation shows a statistically significant (p<0.05) correlation with the observations from CERES (Su et al., 2005) all-sky and clear-sky radiation throughout the year except in MAM and JJAS clear-sky conditions (Figure S26 and S27). Here we didn't separate clear and cloudy days because the aerosol-cloud interactions are absent in the model. Therefore, the

480
481
482
483
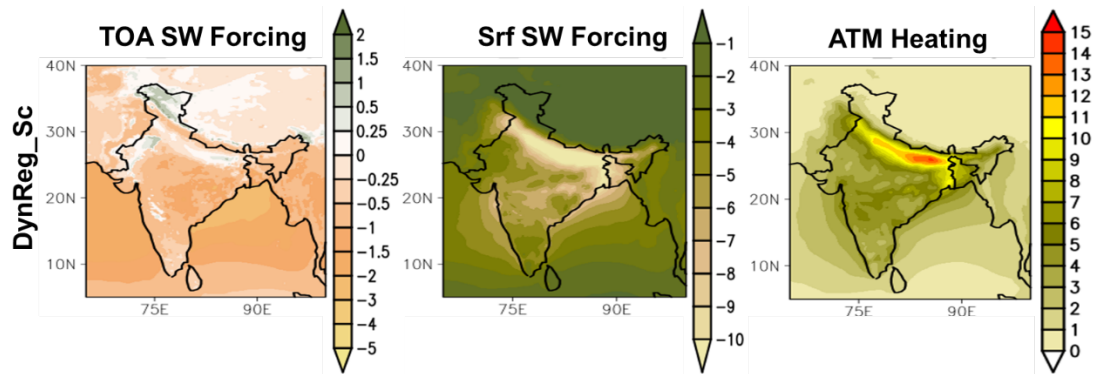
Figure 8 Annual variation of SW radiative forcing (W m^{-2}) at TOA (left column), at the surface (middle column), and the resultant atmospheric heating (W/m^2) (right column) for the customized set-up.

4 Discussion and conclusions

Accurate estimates of emission fluxes and a better representation of aerosol processes are required to improve the representation of aerosol life-cycle and radiative effects in climate models. Here we modified the regional climate model RegCM4 by implementing a dynamic ageing scheme and a regional emission inventory and examined the combined impact of these factors on the model performance over the Indian monsoon region. We note that though the aerosol simulations improve due to these model enhancements, some systematic biases persist (underestimation of carbonaceous aerosol concentrations) and need to be further addressed. For example, RegCM has a bulk scheme for anthropogenic aerosols, and thus the number concentration is calculated from the bulk mass concentration (Ghosh et al., 2021). The anthropogenic aerosol module can thus be improved by including a particle size-dependent representation. In addition, the present dynamic ageing timescale depends only on the anthropogenic aerosol number concentration, while it should, in fact, depend on the total (anthropogenic + natural) number concentrations. The simulations presented in this work did not include natural aerosols, which could have impacted the meteorology through dynamic feedback, possibly affecting the carbonaceous aerosol burden. This aspect will be examined in

future work. Thirdly, though the emission fluxes of BC, OC, and SO_2 are higher in the region than the global inventory, there may still be uncertainty related to missing sectoral sources.

Our work demonstrates that even the improvement of some aspects of the aerosol representation can lead to substantial enhancements in the model performance. We also find that over the South Asian monsoon region, particularly over highly polluted regions such as the IGP, the default model significantly underestimates the surface dimming and atmospheric heating, which can have implications for climate studies (Das et al., 2016, 2020) and this problem is substantially ameliorated with our model augmentations.

The key conclusions of our work can be summarized as follows.

1. The conclusion in the model RegCM4 of a dynamic ageing scheme and a regional emission inventory substantially improves the model performance over the Indian sub-continent.

2. The BC and OC surface concentration and column burden increase due to the model improvements, more so as a combined effect of the two factors than because of the individual ones.

3. The TOA, surface, and atmospheric radiative forcing are estimated to be -0.3, -5.3, and 5.0 W m^{-2}, respectively, over the polluted IGP using the augmented model, but they could still be underestimated.

Data availability. The model RegCM4 code is freely available online from (https://gforge.ictp.it/gf/project/regcm/). The anthropogenic aerosol emissions considered for the simulations are taken from the IIASA inventory. The data used can be easily accessed online at http://clima-dods.ictp.it/Data/RegCM_Data/RCP_EMGLOB_PROCESSED/iiasa/ website. Input files for the RegCM4 model are archived on http://clima-dods.ictp.it/Data/RegCM_Data/ website. MISR data is available freely from https://www-misr.jpl.nasa.gov/ while MERRA-2 data is freely available from the NASA Giovanni site https://giovanni.gsfc.nasa.gov/giovanni/.

Competing Interests. All the authors declare that they have no conflict of interest.

Acknowledgements. We thank the Aerosol Radiative Forcing over India (ARFINET) project of ISRO GBP for sharing the BC data. The authors thank the internal review committee of the NCAP-COALESCE project for their comments and suggestions. The views expressed in this

539 document are solely those of the authors and do not necessarily reflect those of the Ministry.

540 The Ministry does not endorse any products or commercial services mentioned in this

541 publication. SG acknowledges the supercomputing facility Keeling of the University of Illinois

542 Urbana-Champaign. SD acknowledges IIT Delhi for the support for the Institute Chair

543 fellowship.

544

545 *Financial Support.* This work is supported by the MoEFCC under the NCAP-COALESCE

546 project [Grant 14/10/2014-CC]. SG acknowledges the support for the DST-INSPIRE

547 fellowship (IF150055) and Fulbright-Kalam Climate Doctoral Fellowship. NR acknowledges

548 funding from NSF AGS-1254428 and DOE grant DE-SC0019192. Funding from the

549 Department of Science and Technology – Funds for Improvement of Science and Technology

550 infrastructure in universities and higher educational institutions (DST-FIST) grant

551 (SR/FST/ESII-016/2014) is acknowledged for the computing support.

552

References

554

555 Ajay, P., Pathak, B., Solmon, F., Bhuyan, P. K., and Giorgi, F.: Obtaining best parameterization scheme
556 of RegCM 4.4 for aerosols and chemistry simulations over the CORDEX South Asia, 53, 329–352,
557 https://doi.org/10.1007/s00382-018-4587-3, 2019.

558 Babu, S. S., Manoj, M. R., Moorthy, K. K., Gogoi, M. M., Nair, V. S., Kompalli, S. K., Satheesh, S. K.,
559 Niranjan, K., Ramagopal, K., Bhuyan, P. K., and Singh, D.: Trends in aerosol optical depth over Indian
560 region: Potential causes and impact indicators, 118, 11,794-11,806,
561 https://doi.org/10.1002/2013JD020507, 2013.

562 Bond, T. C., Doherty, S. J., Fahey, D. W., Forster, P. M., Berntsen, T., Deangelo, B. J., Flanner, M. G.,
563 Ghan, S., Kärcher, B., Koch, D., Kinne, S., Kondo, Y., Quinn, P. K., Sarofim, M. C., Schultz, M. G.,
564 Schulz, M., Venkataraman, C., Zhang, H., Zhang, S., Bellouin, N., Guttikunda, S. K., Hopke, P. K.,
565 Jacobson, M. Z., Kaiser, J. W., Klimont, Z., Lohmann, U., Schwarz, J. P., Shindell, D., Storelvmo, T.,
566 Warren, S. G., and Zender, C. S.: Bounding the role of black carbon in the climate system: A scientific
567 assessment, 118, 5380–5552, https://doi.org/10.1002/jgrd.50171, 2013.

568 Bretherton, C. S., McCaa, J. R., and Grenier, H.: A New Parameterization for Shallow Cumulus
569 Convection and Its Application to Marine Subtropical Cloud-Topped Boundary Layers. Part I:
570 Description and 1D Results, 132, 864–882, https://doi.org/10.1175/1520-
571 0493(2004)132<0864:ANPFSC>2.0.CO;2, 2004.

572 Buchard, V., Randles, C. A., Silva, A. M. da, Darmenov, A., Colarco, P. R., Govindaraju, R., Ferrare, R.,
573 Hair, J., Beyersdorf, A. J., Ziemba, L. D., and Yu, H.: The MERRA-2 Aerosol Reanalysis, 1980 Onward.
574 Part II: Evaluation and Case Studies, 30, 6851–6872, https://doi.org/10.1175/JCLI-D-16-0613.1, 2017.

575   Das, S., Dey, S., Dash, S. K., Giuliani, G., and Solmon, F.: Dust aerosol feedback on the Indian summer
576   monsoon: Sensitivity to absorption property, 120, 9642–9652,
577   https://doi.org/10.1002/2015JD023589, 2015.

578   Das, S., Dey, S., and Dash, S. K.: Direct radiative effects of anthropogenic aerosols on Indian summer
579   monsoon circulation, 124, 629–639, https://doi.org/10.1007/s00704-015-1444-8, 2016.

580   Das, S., Giorgi, F., Giuliani, G., Dey, S., and Coppola, E.: Near-Future Anthropogenic Aerosol Emission
581   Scenarios and Their Direct Radiative Effects on the Present-Day Characteristics of the Indian Summer
582   Monsoon, 125, https://doi.org/10.1029/2019JD031414, 2020.

583   Dash, S. K., Mishra, S. K., Pattnayak, K. C., Mamgain, A., Mariotti, L., Coppola, E., Giorgi, F., and
584   Giuliani, G.: Projected seasonal mean summer monsoon over India and adjoining regions for the
585   twenty-first century, Theor Appl Climatol, 122, 581–593, https://doi.org/10.1007/s00704-014-1310-
586   0, 2015.

587   Dee, D. P., Uppala, S. M., Simmons, A. J., Berrisford, P., Poli, P., Kobayashi, S., Andrae, U., Balmaseda,
588   M. A., Balsamo, G., Bauer, P., Bechtold, P., Beljaars, A. C. M., van de Berg, L., Bidlot, J., Bormann, N.,
589   Delsol, C., Dragani, R., Fuentes, M., Geer, A. J., Haimberger, L., Healy, S. B., Hersbach, H., Hólm, E. V.,
590   Isaksen, L., Kållberg, P., Köhler, M., Matricardi, M., Mcnally, A. P., Monge-Sanz, B. M., Morcrette, J. J.,
591   Park, B. K., Peubey, C., de Rosnay, P., Tavolato, C., Thépaut, J. N., and Vitart, F.: The ERA-Interim
592   reanalysis: Configuration and performance of the data assimilation system, 137, 553–597,
593   https://doi.org/10.1002/qj.828, 2011.

594   Dey, S. and Di Girolamo, L.: A climatology of aerosol optical and microphysical properties over the
595   Indian subcontinent from 9 years (2000–2008) of Multiangle Imaging Spectroradiometer (MISR)
596   data, 115, https://doi.org/10.1029/2009JD013395, 2010.

597   Dickinson, R., Henderson-Sellers, A., and Kennedy, P.: Biosphere-atmosphere Transfer Scheme
598   (BATS) Version 1e as Coupled to the NCAR Community Climate Model, UCAR/NCAR,
599   https://doi.org/10.5065/D67W6959, 1993.

600   Diner, D. J., Beckert, J. C., Reilly, T. H., Bruegge, C. J., Conel, J. E., Kahn, R. A., Martonchik, J. V.,
601   Ackerman, T. P., Davies, R., Gerstl, S. A. W., Gordon, H. R., Muller, J.-P., Myneni, R. B., Sellers, P. J.,
602   Pinty, B., and Verstraete, M. M.: Multi-angle Imaging SpectroRadiometer (MISR) instrument
603   description and experiment overview, 36, 1072–1087, https://doi.org/10.1109/36.700992, 1998.

604   Emanuel, K. A. and Živković-Rothman, M.: Development and Evaluation of a Convection Scheme for
605   Use in Climate Models, 56, 1766–1782, https://doi.org/10.1175/1520-
606   0469(1999)056<1766:DAEOAC>2.0.CO;2, 1999.

607   Gadhavi, H. S., Renuka, K., Ravi Kiran, V., Jayaraman, A., Stohl, A., Klimont, Z., and Beig, G.:
608   Evaluation of black carbon emission inventories using a Lagrangian dispersion model – a case study
609   over southern India, 15, 1447–1461, https://doi.org/10.5194/acp-15-1447-2015, 2015.

610   Ghosh, S., Riemer, N., Giuliani, G., Giorgi, F., Ganguly, D., and Dey, S.: Sensitivity of Carbonaceous
611   Aerosol Properties to the Implementation of a Dynamic Aging Parameterization in the Regional
612   Climate Model RegCM, 126, e2020JD033613, https://doi.org/10.1029/2020JD033613, 2021.

613   Giorgi, F., Jones, C., and Asrar, G. R.: Addressing climate information needs at the regional level: the
614   CORDEX framework, WMO Bulletin, 2009.

Giorgi, F., Coppola, E., Solmon, F., Mariotti, L., Sylla, M. B., Bi, X., Elguindi, N., Diro, G. T., Nair, V., Giuliani, G., Turuncoglu, U. U., Cozzini, S., Güttler, I., O'Brien, T. A., Tawfik, A. B., Shalaby, A., Zakey, A. S., Steiner, A. L., Stordal, F., Sloan, L. C., and Brankovic, C.: RegCM4: Model description and preliminary tests over multiple CORDEX domains, 52, 7–29, https://doi.org/10.3354/cr01018, 2012.

Gogoi, M. M., Babu, S. S., Arun, B. S., Moorthy, K. K., Ajay, A., Ajay, P., Suryavanshi, A., Borgohain, A., Guha, A., Shaikh, A., Pathak, B., Gharai, B., Ramasamy, B., Balakrishnaiah, G., Menon, H. B., Kuniyal, J. C., Krishnan, J., Gopal, K. R., Maheswari, M., Naja, M., Kaur, P., Bhuyan, P. K., Gupta, P., Singh, P., Srivastava, P., Singh, R. S., Kumar, R., Rastogi, S., Kundu, S. S., Kompalli, S. K., Panda, S., Rao, T. C., Das, T., and Kant, Y.: Response of ambient BC concentration across the Indian region to the nation-wide lockdown: results from the ARFINET measurements of, 120, 11, 2021.

Grell, G., Dudhia, J., and Stauffer, D.: A description of the fifth-generation Penn State/NCAR Mesoscale Model (MM5), UCAR/NCAR, https://doi.org/10.5065/D60Z716B, 1994.

Grenier, H. and Bretherton, C. S.: A Moist PBL Parameterization for Large-Scale Models and Its Application to Subtropical Cloud-Topped Marine Boundary Layers, 129, 357–377, https://doi.org/10.1175/1520-0493(2001)129<0357:AMPPFL>2.0.CO;2, 2001.

Hansen, A. D. A., Rosen, H., and Novakov, T.: The aethalometer — An instrument for the real-time measurement of optical absorption by aerosol particles, Science of The Total Environment, 36, 191–196, https://doi.org/10.1016/0048-9697(84)90265-1, 1984.

Jain, C. D., Gadhavi, H. S., Wankhede, T., Kallelapu, K., Sudhesh, S., Das, L. N., Pai, R. U., and Jayaraman, A.: Spectral Properties of Black Carbon Produced during Biomass Burning, Aerosol Air Qual. Res., 18, 671–679, https://doi.org/10.4209/aaqr.2017.03.0102, 2018.

Kahn, R., Li, W.-H., Martonchik, J. V., Bruegge, C. J., Diner, D. J., Gaitley, B. J., Abdou, W., Dubovik, O., Holben, B., Smirnov, A., Jin, Z., and Clark, D.: MISR Calibration and Implications for Low-Light-Level Aerosol Retrieval over Dark Water, 62, 1032–1052, https://doi.org/10.1175/JAS3390.1, 2005.

Kahn, R. A. and Gaitley, B. J.: An analysis of global aerosol type as retrieved by MISR, 120, 4248–4281, https://doi.org/10.1002/2015JD023322, 2015.

Kanakidou, M., Seinfeld, J. H., Pandis, S. N., Barnes, I., Dentener, F. J., Facchini, M. C., Van Dingenen, R., Ervens, B., Nenes, A., Nielsen, C. J., Swietlicki, E., Putaud, J. P., Balkanski, Y., Fuzzi, S., Horth, J., Moortgat, G. K., Winterhalter, R., Myhre, C. E. L., Tsigaridis, K., Vignati, E., Stephanou, E. G., and Wilson, J.: Organic aerosol and global climate modelling: a review, 5, 1053–1123, https://doi.org/10.5194/acp-5-1053-2005, 2005.

Kiehl, J., Hack, J., Bonan, G., Boville, B., Briegleb, B., Williamson, D., and Rasch, P.: Description of the NCAR Community Climate Model (CCM3), UCAR/NCAR, https://doi.org/10.5065/D6FF3Q99, 1996.

Naik, V., Szopa, S., Adhikary, B., Artaxo Netto, P. E., Berntsen, T., Collins, W. D., Fuzzi, S., Gallardo, L., Kiendler-Scharr, A., Klimont, Z., Liao, H., Unger, N., and Zanis, P.: Short-lived climate forcers, in: Climate Change 2021: The Physical Science Basis. Contribution of Working Group I to the Sixth Assessment Report of the Intergovernmental Panel on Climate Change, edited by: Masson-Delmotte, V., Zhai, P., Pirani, A., Connors, S. L., Péan, C., Berger, S., Caud, N., Chen, Y., Goldfarb, L., Gomis, M. I., Huang, M., Leitzell, K., Lonnoy, E., Matthews, J. B. R., Maycock, T. K., Waterfield, T., Yelekçi, Ö., Yu, R., and Zhou, B., Cambridge University Press, 2021.

Nair, V. S., Solmon, F., Giorgi, F., Mariotti, L., Babu, S. S., and Moorthy, K. K.: Simulation of South Asian aerosols for regional climate studies, 117, 4209, https://doi.org/10.1029/2011JD016711, 2012.

657   O'Brien, T. A., Chuang, P. Y., Sloan, L. C., Faloona, I. C., and Rossiter, D. L.: Coupling a new turbulence
658   parametrization to RegCM adds realistic stratocumulus clouds, 5, 989–1008,
659   https://doi.org/10.5194/gmd-5-989-2012, 2012.

660   Pal, J. S., Small, E. E., and Eltahir, E. A. B.: Simulation of regional-scale water and energy budgets:
661   Representation of subgrid cloud and precipitation processes within RegCM, 105, 29579–29594,
662   https://doi.org/10.1029/2000JD900415, 2000.

663   Pal, J. S., Giorgi, F., Bi, X., Elguindi, N., Solmon, F., Gao, X., Rauscher, S. A., Francisco, R., Zakey, A.,
664   Winter, J., Ashfaq, M., Syed, F. S., Bell, J. L., Differbaugh, N. S., Karmacharya, J., Konari, A., Martinez,
665   D., Da Rocha, R. P., Sloan, L. C., and Steiner, A. L.: Regional Climate Modeling for the Developing
666   World: The ICTP RegCM3 and RegCNET, 88, 1395–1410, https://doi.org/10.1175/BAMS-88-9-1395,
667   2007.

668   Pandey, A. and Venkataraman, C.: Estimating emissions from the Indian transport sector with on-
669   road fleet composition and traffic volume, Atmospheric Environment, 98, 123–133,
670   https://doi.org/10.1016/j.atmosenv.2014.08.039, 2014.

671   Pattnayak, K. C., Panda, S. K., Saraswat, V., and Dash, S. K.: Assessment of two versions of regional
672   climate model in simulating the Indian Summer Monsoon over South Asia CORDEX domain, 50,
673   3049–3061, https://doi.org/10.1007/s00382-017-3792-9, 2018.

674   Priyadharshini, B., Verma, S., Chatterjee, A., Sharma, S. K., and Mandal, T. K.: Chemical
675   characterization of fine atmospheric particles of water-soluble ions and carbonaceous species in a
676   tropical urban atmosphere over the eastern Indo-Gangetic plain, 19, 129–147,
677   https://doi.org/10.4209/aaqr.2017.12.0606, 2019.

678   Putaud, J.-P., Van Dingenen, R., Alastuey, A., Bauer, H., Birmili, W., Cyrys, J., Flentje, H., Fuzzi, S.,
679   Gehrig, R., Hansson, H. C., Harrison, R. M., Herrmann, H., Hitzenberger, R., Hüglin, C., Jones, A. M.,
680   Kasper-Giebl, A., Kiss, G., Kousa, A., Kuhlbusch, T. A. J., Löschau, G., Maenhaut, W., Molnar, A.,
681   Moreno, T., Pekkanen, J., Perrino, C., Pitz, M., Puxbaum, H., Querol, X., Rodriguez, S., Salma, I.,
682   Schwarz, J., Smolik, J., Schneider, J., Spindler, G., ten Brink, H., Tursic, J., Viana, M., Wiedensohler, A.,
683   and Raes, F.: A European aerosol phenomenology – 3: Physical and chemical characteristics of
684   particulate matter from 60 rural, urban, and kerbside sites across Europe, Atmospheric Environment,
685   44, 1308–1320, https://doi.org/10.1016/j.atmosenv.2009.12.011, 2010.

686   Qian1, Y., Giorgi1, F., Huang2, Y., Chameides2, W., and Luo2, C.: Regional simulation of
687   anthropogenic sulfur over East Asia and its sensitivity to model parameters, 53, 171–191, 2001.

688   Rai, P. K., Singh, G. P., and Dash, S. K.: Projected Change and Variability Assessment of Indian
689   Summer Monsoon Precipitation in South Asia CORDEX Domain Under High-Emission Pathway, 177,
690   3475–3499, https://doi.org/10.1007/s00024-019-02373-3, 2020.

691   Ram, K., Sarin, M. M., and Tripathi, S. N.: A 1 year record of carbonaceous aerosols from an urban
692   site in the Indo-Gangetic Plain: Characterization, sources, and temporal variability, 115,
693   https://doi.org/10.1029/2010JD014188, 2010.

694   Ramanathan, V. and Carmichael, G.: Global and regional climate changes due to black carbon, 1,
695   221–227, https://doi.org/10.1038/ngeo156, 2008.

696   Riemer, N., Ault, A. P., West, M., Craig, R. L., and Curtis, J. H.: Aerosol Mixing State: Measurements,
697   Modeling, and Impacts, 57, 187–249, https://doi.org/10.1029/2018RG000615, 2019.

698   Sadavarte, P. and Venkataraman, C.: Trends in multi-pollutant emissions from a technology-linked
699   inventory for India: I. Industry and transport sectors, Atmospheric Environment, 99, 353–364,
700   https://doi.org/10.1016/j.atmosenv.2014.09.081, 2014.

701   Satheesh, S. K.: *Letter to the Editor*
Aerosol radiative forcing over land: effect of surface and
702   cloud reflection, 20, 2105–2109, https://doi.org/10.5194/angeo-20-2105-2002, 2002.

703   Shalaby, A., Zakey, A. S., Tawfik, A. B., Solmon, F., Giorgi, F., Stordal, F., Sillman, S., Zaveri, R. A., and
704   Steiner, A. L.: Implementation and evaluation of online gas-phase chemistry within a regional climate
705   model (RegCM-CHEM4), 5, 741–760, https://doi.org/10.5194/GMD-5-741-2012, 2012.

706   Singh, A., Rastogi, N., Kumar, V., Slowik, J. G., Satish, R., Lalchandani, V., Thamban, N. M., Rai, P.,
707   Bhattu, D., Vats, P., Ganguly, D., Tripathi, S. N., and Prévôt, A. S. H.: Sources and characteristics of
708   light-absorbing fine particulates over Delhi through the synergy of real-time optical and chemical
709   measurements, Atmospheric Environment, 252, 118338,
710   https://doi.org/10.1016/j.atmosenv.2021.118338, 2021.

711   Solmon, F., Giorgi, F., and Liousse, C.: Aerosol modelling for regional climate studies: Application to
712   anthropogenic particles and evaluation over a European/African domain, 58, 51–72,
713   https://doi.org/10.1111/j.1600-0889.2005.00155.x, 2006.

714   Srivastava, A. K., Dey, S., and Tripathi, S. N.: Aerosol Characteristics over the Indo-Gangetic Basin:
715   Implications to Regional Climate, IntechOpen, https://doi.org/10.5772/47782, 2012.

716   Su, W., Charlock, T. P., and Rose, F. G.: Deriving surface ultraviolet radiation from CERES surface and
717   atmospheric radiation budget: Methodology, 110, https://doi.org/10.1029/2005JD005794, 2005.

718   Tibrewal, K. and Venkataraman, C.: Climate co-benefits of air quality and clean energy policy in India,
719   4, 305–313, https://doi.org/10.1038/s41893-020-00666-3, 2021.

720   Tiedtke, M.: Representation of Clouds in Large-Scale Models, 121, 3040–3061,
721   https://doi.org/10.1175/1520-0493(1993)121<3040:ROCILS>2.0.CO;2, 1993.

722   Tripathi, S. N., Dey, S., Tare, V., Satheesh, S. K., Lal, S., and Venkataramani, S.: Enhanced layer of
723   black carbon in a north Indian industrial city, 32, https://doi.org/10.1029/2005GL022564, 2005.

724   Venkataraman, C.: Supplement of Source influence on emission pathways and ambient PM 2.5
725   pollution over India (2015-2050) The copyright of individual parts of the supplement might differ
726   from the CC BY 4.0 License, 18, 8017–8039, https://doi.org/10.5194/acp-18-8017-2018-supplement,
727   2018.

728   Venkataraman, C., Brauer, M., Tibrewal, K., Sadavarte, P., Ma, Q., Cohen, A., Chaliyakunnel, S.,
729   Frostad, J., Klimont, Z., Martin, R. V., Millet, D. B., Philip, S., Walker, K., and Wang, S.: Source
730   influence on emission pathways and ambient PM2.5 pollution over India (2015-2050), 18, 8017–
731   8039, https://doi.org/10.5194/acp-18-8017-2018, 2018.

732   Venkataraman, C., Bhushan, M., Dey, S., Ganguly, D., Gupta, T., Habib, G., Kesarkar, A., Phuleria, H.,
733   and Sunder Raman, R.: Indian network project on carbonaceous aerosol emissions, source
734   apportionment and climate impacts (COALESCE), 101, E1052–E1068, https://doi.org/10.1175/BAMS-
735   D-19-0030.1, 2020.

736   Zakey, A. S., Solmon, F., and Giorgi, F.: Implementation and testing of a desert dust module in a
737   regional climate model, Atmos. Chem. Phys, 2006.

738   Zakey, A. S., Giorgi, F., and Bi, X.: Modeling of sea salt in a regional climate model: Fluxes and
739   radiative forcing, 113, 14221, https://doi.org/10.1029/2007JD009209, 2008.

740